

Cite this: *J. Mater. Chem. A*, 2017, 5, 16568Received 13th June 2017
Accepted 13th July 2017

DOI: 10.1039/c7ta05146h

rsc.li/materials-a

Nitrogen-doped carbon nanocones encapsulating with nickel–cobalt mixed phosphides for enhanced hydrogen evolution reaction†

Lei Han, Tongwen Yu, Wen Lei, Wenwen Liu, Kun Feng, Yuanli Ding, Gaopeng Jiang, Pan Xu and Zhongwei Chen *

In this work, nickel–cobalt mixed metal phosphides encapsulated into nitrogen-doped carbon nanocones ($\text{Ni}_2\text{P}/\text{NiCoP}@N\text{CCs}$) have been prepared through a facile ammonia-etching of nickel–cobalt Prussian blue analogs (Ni–Co PBAs) followed by a subsequent phosphidation treatment. During the *in situ* and confined phosphidation process, very small nickel–cobalt mixed metal phosphide nanocrystallites are uniformly incorporated into the simultaneously produced nitrogen-doped carbon matrix. Due to the unique structure and composition, the resultant $\text{Ni}_2\text{P}/\text{NiCoP}@N\text{CCs}$ possess high electrocatalytic activity and excellent durability for the HER in both acidic and alkaline solutions.

Hydrogen production by electrochemical water splitting is widely regarded as a promising and attractive way to solve the current energy crisis and environmental issues.^{1–8} In order to make this process efficient and practical, it is very necessary and important to exploit highly active catalysts to accelerate the hydrogen evolution reaction (HER). To date, the state-of-the-art HER electrocatalysts are mainly Pt-group noble metals and their alloys due to their high catalytic activity such as low overpotential and fast reaction kinetics.^{9–13} However, their paucity and high cost largely impede their practical applications. Fortunately, some transition-metal-based materials have been demonstrated as promising alternatives to noble-metal HER electrocatalysts, including metal sulfides,^{14,15} metal carbides,^{9,10} metal nitrides,¹⁶ and metal phosphides.^{17–21} Especially, transition-metal phosphides receive much more attention owing to their facile preparation and low cost as well as excellent durability.^{4,22–27} The performances of materials are largely related to their morphologies.^{21,28} Therefore, various methods have been developed to prepare different nanostructured morphologies of transition-metal phosphides, aiming to achieve optimal performances.^{1,2,22,27,29,30} As reported, the most

efficient way to control the morphologies of transition-metal phosphides is to tune the morphology of the corresponding precursors. For instance, nanostructured cobalt oxides with different morphologies, including nanowires, nanosheets and nanoparticles, were first prepared and then converted into CoP *via* a phosphidation route.³¹ In addition, cobalt phosphides with hollow and/or porous concave polyhedron structures have been successfully prepared by heat treatment of zeolitic imidazolate framework-67 (ZIF-67) polyhedra in air with a sequential phosphidation treatment with NaH_2PO_2 .^{19,32} Besides, Zhang *et al.* also reported the preparation of three-dimensional (3D) graphene aerogel decorated with cobalt phosphide nanoparticles through combining self-assembly with freeze-drying and thermal treatment as well as a phosphidation process.¹⁷ Despite the progress, the construction of transition-metal-phosphide precursors with special complex nanostructured morphologies such as nanocones still remains a challenge because of the extreme formation conditions needed.

In the past few years, the chemical etching method has been reported as an efficient method to prepare some special complex nanostructures,^{28,33–35} which can endow these nanostructured materials with unique physicochemical properties. Recently, Yamauchi's group and Lou's group utilized this method to prepare various Prussian blue analogues (PBAs) and/or PBA-derived metal oxides/sulfides with hollow complex nanostructures like hollow nanocubes, nanocages and nanoframes.^{28,35,36} Inspired by them, in the present work, nickel–cobalt Prussian blue analogue (Ni–Co PBA) nanocones were successfully prepared through a facile ammonia-etching method (Fig. 1). In the preparation procedure, we shorten the

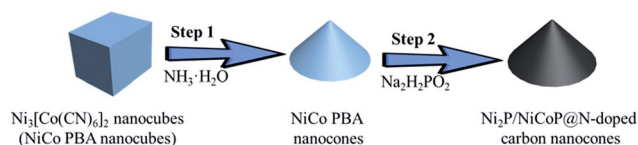


Fig. 1 Schematic of the preparation of $\text{Ni}_2\text{P}/\text{NiCoP}@N$ -doped carbon nanocones (NCCs).

Department of Chemical Engineering, University of Waterloo, 200 University Avenue West, Waterloo, Ontario, N2L3G1, Canada. E-mail: zhwenchen@uwaterloo.ca

† Electronic supplementary information (ESI) available. See DOI: 10.1039/c7ta05146h

precipitation time of Ni–Co PBA nanocubes, thus achieving the successful preparation of Ni–Co PBA nanocones after ammonia-etching (see the ESI for the experimental details[†]). Finally, after the phosphidation treatment of the resultant Ni–Co PBA nanocones in Ar, nickel–cobalt mixed metal phosphides encapsulated into nitrogen-doped carbon nanocones (Ni₂P/NiCoP@NCCs) could be obtained. It should be noted that in our work, the Ni–Co PBA is chosen as the precursor mainly based on the following two reasons. On one hand, as a typical metal–organic framework (MOF), the Ni–Co PBA consists of Ni and Co, which makes it a promising precursor to prepare bimetallic phosphides. Compared to monometallic phosphides, bimetallic phosphides provide two electron-donating active sites to facilitate the proton discharge in the HER process, which helps in enhancing the HER activity.³⁷ On the other hand, encapsulation of active materials into a carbon matrix has been demonstrated as a promising route to improve their HER activity because of the increase in electronic conductivity, avoiding the aggregation and leaching of active materials and the synergistic interaction between the encapsulated active materials and carbon matrix.^{10,38,39} During the phosphidation process in our work, the Ni–Co PBA can be easily converted into nickel–cobalt mixed metal phosphides encapsulated into a nitrogen-doped carbon matrix. These features endow the resultant Ni₂P/NiCoP@NCCs with high HER activity and excellent stability.

Scanning electron microscopy (SEM) and transmission electron microscopy (TEM) were first conducted to characterize the morphology and structure of the resultant Ni–Co PBA. As presented in Fig. 2a and b, the resultant Ni–Co PBA exhibits a cubic morphology with a uniform size of around 400 nm. The crystal structure of the resultant Ni–Co PBA nanotubes is investigated by X-ray diffraction (XRD). All XRD peaks (Fig. 2c) can match well with those of phase-pure Ni₃[Co(CN)₆]₂·xH₂O (JCPDS card no. 89-3738). Energy dispersive X-ray (EDX) analysis results indicate that the composition of the resultant Ni–Co PBA nanocubes consists of Ni, Co, C, and N (Fig. S1a[†]), which is consistent with the XRD result. After reacting with ammonia

solution for 1 h at room temperature, the resultant Ni–Co PBA nanocubes are interestingly converted into cone-like nanoparticles (Fig. 2d–f). It can be seen from Fig. 2d and e that the resultant Ni–Co PBA after ammonia-etching exhibits a uniform nanocone morphology. TEM images (Fig. 2f) also confirm the successful formation of cone-like nanostructures. The composition and crystalline phase of the resultant Ni–Co PBA nanocones are also confirmed by EDX analysis and XRD. As seen, the molar ratio of Ni and Co remains the same as that of the precursor nanocubes (Fig. S1b[†]), and we also interestingly find that all diffraction peaks are also the same as those of the precursor nanocubes (Fig. 2c), which are in accordance with our previously reported results.²⁸ The formation of the unique nanostructures could be explained as follows. As we know, the chemical etching process easily occurs in the defect-rich region, and its rate largely depends on the density of defects.²⁸ In comparison to the flat planes, the corners of the cubes were reported to expose more defects. In addition, the formation of Ni–Co PBA nanocubes is the result of Ostwald ripening, which results in interior defect-rich parts along the diagonals of the cubes.²⁸ So when reacting with ammonia, the cubes are initially etched at their eight corners. As the reaction time prolongs, the diagonals of the cubes begin to be etched, and finally nanocones are obtained with the twelve edges vanish.

The resultant Ni–Co PBA nanocones were further heat-treated with NaH₂PO₂ under Ar. The morphology and structure of the resultant Ni₂P/NiCoP@NCCs are characterized by SEM and TEM, and the results are shown in Fig. 3. It can be seen that the nanocone nanostructures are well maintained in the resultant Ni₂P/NiCoP@NCCs (Fig. 3a–c). The high-resolution TEM images (Fig. 3d and e) indicate that very small Ni₂P/NiCoP nanoparticles are successfully uniformly encapsulated into the produced continuous carbon matrix. Scanning TEM and EDX mapping were also carried out to unravel the morphology and elemental distribution. It can be easily observed that the four elements including C, Ni, Co, and P are uniformly distributed in the resultant Ni₂P/NiCoP@NCCs (Fig. 3f–j), which is in accordance with the EDX results (Fig. S1d[†]). The XRD pattern reveals that the resultant product after phosphidation treatment consists of Ni₂P (JCPDS card no.

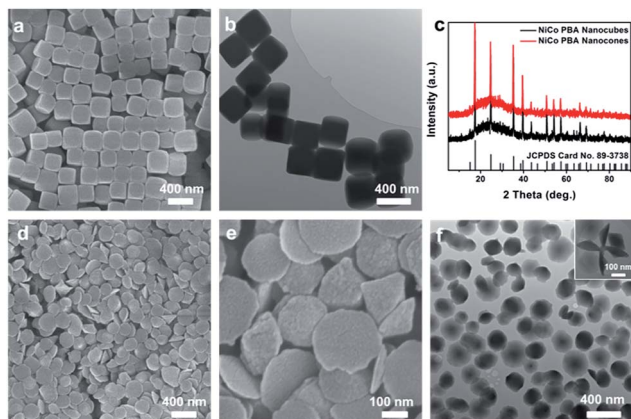


Fig. 2 (a, d and e) SEM images, (b and f) TEM images and (c) Powder XRD patterns of the resultant NiCo PBA nanocubes (a–c) and NiCo PBA nanocones (c–f).

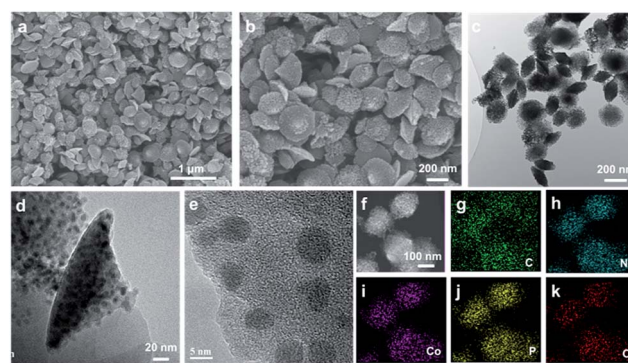


Fig. 3 (a and b) SEM images, (c and d) TEM images, (e) HRTEM, (f) HAADF-STEM and (g–k) elemental mapping images of the resultant Ni₂P/NiCoP@NCCs.

89-2742) and NiCoP (JCPDS card no. 71-2336) (Fig. S3†), and no peaks corresponding to NiCo₂O₄ were observed. Besides, there is a broad diffraction peak at 25°, which can be assigned to the (002) plane of the hexagonal graphitic structure of carbon.⁴⁰ The Raman spectra result (Fig. S4†) also confirms the existence of carbon, where there are two bands centered at 1340 and 1555 cm⁻¹ related to the disorders of the graphite (D-band) and the sp² carbon bonded graphitic structures (G-band), respectively.⁴⁰ For comparison, the resultant Ni-Co PBA nanocubes were also directly heat-treated with NaH₂PO₂ under Ar. SEM and TEM images reveal that the resultant product retains well a cubic morphology with hollow structures (Fig. S2†). Besides, the XRD result confirms that its composition also contains Ni₂P and NiCoP (Fig. S3†). Hereafter this product is labeled Ni₂P/NiCoP@NHCCs for simplicity's sake.

XPS spectra were further obtained to analyze the surface elemental composition and the valence states in the resultant Ni₂P/NiCoP@NHCCs. The XPS survey spectra in Fig. S5a† show the existence of Co, Ni, P, C, N, and O elements in the resultant Ni₂P/NiCoP@NHCCs. The high-resolution XPS spectra of Co 2p, Ni 2p, P 2p, C 1s, N 1s, and O 1s are shown in Fig. S5b–g.† In the Co 2p spectra (Fig. S5b†), the peaks at 778.9 and 781.9 eV are assigned to Co 2p_{3/2}, while the peak located at 786.1 eV is ascribed to the satellite peak of Co 2p_{3/2}. The Co 2p_{1/2} region also shows two main peaks at 793.5 and 798.1 eV and one satellite peak at 803 eV. For Co 2p_{3/2}, the peak at 778.9 eV belongs to Co–P. The peak at 781.9 eV could be attributed to a Co oxidized state, which is related to Co-PO_x. In the Ni 2p spectra (Fig. S5c†), the peaks at 856.9 eV and 861.6 eV are assigned to the oxidized Ni species and the satellite of the Ni 2p_{3/2}, respectively. The other peaks at 874.8 eV and 880.2 eV correspond to oxidized Ni species, and the satellite of the Ni 2p_{1/2}, respectively. As shown in Fig. S5d,† there are two peaks at 129.3 eV and 134 eV in the P 2p spectra, which stand for reduced phosphorus in metal phosphides and phosphate species resulting from the oxidation of metal phosphides after exposure to air, respectively. To further demonstrate the oxidized Co/Ni, the O 1s binding energy is shown in Fig. S5g.† As shown, there are also two peaks at 531.5 eV and 533 eV, which belong to either MO_x or M(OH)_x (M = Co, Ni) and oxidized phosphate species, respectively. Fig. S5f† shows the XPS spectra of N 1s, where the peaks at 398.9, 400, and 401 eV can be attributed to pyridinic-N, pyrrolic-N, and quaternary-N, respectively. The C 1s spectra (Fig. S5e†) also show three peaks at 284.6, 286.2, and 288.9 eV, which are ascribed to sp²-C, -C-O-, and -C=O, respectively. All of these XPS data confirm the successful synthesis of Ni₂P/NiCoP@NHCCs.

The HER activities of the resultant products including Ni₂P/NiCoP@NCCs and Ni₂P/NiCoP@NHCCs were evaluated in a three-electrode configuration, where a graphite rod and saturated calomel electrode (SCE) are used as the counter electrode and reference electrode, respectively. The effect of the loading amount of the catalyst on the HER activity was first investigated. It can be clearly noticed from Fig. S6† that the resultant Ni₂P/NiCoP@NCCs exhibit the highest HER activity when the loading amount is 0.5 mg cm⁻². Therefore the loading amount is fixed at 0.5 mg cm⁻² in the later experiment. Then we

compared the HER activity of the resultant Ni₂P/NiCoP@NCCs and Ni₂P/NiCoP@NHCCs. Fig. 4a exhibits the polarization curves of the resultant Ni₂P/NiCoP@NCCs and Ni₂P/NiCoP@NHCCs in 1.0 M KOH. Obviously, the resultant Ni₂P/NiCoP@NCCs show a lower onset potential and higher current density towards the HER than the resultant Ni₂P/NiCoP@NHCCs. In particular, at a current density of 10 mA cm⁻², the overpotential of the resultant Ni₂P/NiCoP@NCCs (116 mV) is lower by 52 mV than that of the resultant Ni₂P/NiCoP@NHCCs (168 mV). Moreover, the HER performance is superior to that of other reported bimetallic phosphides such as NiCoP hollow polyhedra and CuCoP/nitrogen-doped carbon (see Table S1†).^{18,20} At the same time, the kinetic behaviors of the resultant Ni₂P/NiCoP@NCCs and Ni₂P/NiCoP@NHCCs are also further investigated by using Tafel plots derived from Fig. 4a according to the Tafel equation ($\eta = b \log j + a$, where η is the overpotential, j is the current density, and b is the Tafel slope). As displayed in Fig. 4b, the Tafel slope of the resultant Ni₂P/NiCoP@NCCs (79 mV dec⁻¹) is slightly smaller than that of the resultant Ni₂P/NiCoP@NHCCs (89 mV dec⁻¹), indicating the improved HER kinetics over the resultant Ni₂P/NiCoP@NCCs. As for stability, it is also important for practical application. So a recycling CV or LSV experiment was performed to evaluate the stability of the resultant catalysts. Fig. 4c shows the polarization curves of the resultant Ni₂P/NiCoP@NCCs before and after 1000 continuous cyclic voltammetry (CV) cycles at a scan rate of 100 mV s⁻¹ between 0.05 V and -0.257 V (vs. the RHE). No obvious change of the HER activity is observed, revealing the good stability of the resultant Ni₂P/NiCoP@NCCs. On the other hand, the HER activity of the resultant catalysts was also evaluated in 0.5 M H₂SO₄, and the results are displayed in Fig. 4d–f. The HER activity of the resultant Ni₂P/NiCoP@NCCs also outperforms obviously that of the resultant Ni₂P/NiCoP@NHCCs, including lower onset potential and higher current density (Fig. 4d). An overpotential of only 120 mV is required for the resultant Ni₂P/NiCoP@NCCs to achieve the current density of 10 mA cm⁻², which is lower

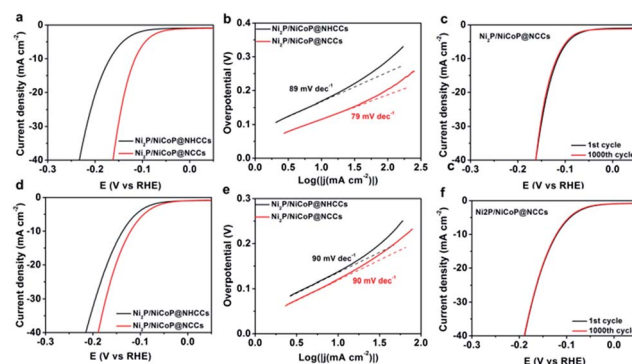


Fig. 4 Electrochemical evaluation of the resultant Ni₂P/NiCoP@NHCCs and Ni₂P/NiCoP@NCCs in 1.0 M NaOH (a–c) and 0.5 M H₂SO₄ (d–f) with a loading amount of 0.5 mg cm⁻². (a–d) polarization curves with *iR*-correction of the GC electrode at 5 mV s⁻¹, (b–e) Tafel slopes, and (c–f) polarization curves with *iR*-correction of Ni₂P/NiCoP@NCCs before and after 1000 cycles at a scan rate of 100 mV s⁻¹ between 0.05 V and -0.233 V.

than that of the resultant Ni₂P/NiCoP@NHCCs (136 mV) and outperforms the reported other metal phosphides such as porous CoP concave polyhedra and porous Ni₂P polyhedra (see Table S1†).^{19,41} Fig. 4e displays the Tafel plot of the resultant Ni₂P/NiCoP@NCCs and Ni₂P/NiCoP@NHCCs, where the same Tafel slope (79 mV dec⁻¹) can be observed. Moreover, the resultant Ni₂P/NiCoP@NCCs also possess good stability in 0.5 M H₂SO₄ (Fig. 4f). Generally, the HER process involves the following steps in an acidic solution: the Volmer step (116 mV dec⁻¹), the Heyrovsky step (38 mV dec⁻¹), or the Tafel step (29 mV dec⁻¹).¹⁹ Therefore, the Tafel slope of the resultant Ni₂P/NiCoP@NCCs indicates that the corresponding HER follows a Volmer–Heyrovsky mechanism. However, the large Tafel slope herein may be further optimized by altering the annealing temperature and the mass ratio of NiCo PBA and NaH₂PO₂.

In order to get insight into the enhanced HER activity, we first measured the Brunauer–Emmett–Teller (BET) surface area (Fig. S7†). As can be noted, the BET surface area of the resultant Ni₂P/NiCoP@NCCs (67.3 m² g⁻¹) is higher than that of the resultant Ni₂P/NiCoP@NHCCs (29.2 m² g⁻¹), which is beneficial for improving the HER activity. Then electrochemical impedance spectroscopy (EIS) was also performed to investigate the interfacial behavior of the resultant Ni₂P/NiCoP@NCCs and Ni₂P/NiCoP@NHCCs modified electrodes (Fig. S8†). It can be seen that the resultant Ni₂P/NiCoP@NCCs show a smaller electron-transfer resistance than the resultant Ni₂P/NiCoP@NHCCs, which may help to enhance the HER activity. Finally the electrochemically active surface area (ECSA) was estimated according to the electrochemical double-layer capacitance (C_{dl}).²⁸ Based on this point, CV curves at different scan rates in the potential range without the redox process were obtained. As presented in Fig. S9 and S10,† the resultant Ni₂P/NiCoP@NCCs and Ni₂P/NiCoP@NHCCs both have almost the same ECSA. Therefore, the enhanced HER activity could be attributed to the synergistic effect of the large BET surface area and small electron-transfer resistance.

In summary, we have successfully prepared Ni₂P/NiCoP@NCCs through a facile ammonia-etching and phosphidation treatment using Ni–Co PBA nanocubes as the precursor. The *in situ* and confined phosphidation process leads to the formation of very small Ni₂P/NiCoP nanocrystallites encapsulated uniformly into the generated nitrogen-doped carbon matrix. When used as HER electrocatalysts, the resultant Ni₂P/NiCoP@NCCs exhibit high electrocatalytic activity in both alkaline and acidic solutions with low overpotential at a current density of 10 mA cm⁻² and good stability owing to their unique structure and morphology.

Acknowledgements

This research was supported by the Natural Sciences and Engineering Research Council of Canada (NSERC). TEM was obtained at the Canadian Center for Electron Microscopy (CCEM) located at McMaster University.

Notes and references

- H. Yang, Y. Zhang, F. Hu and Q. Wang, *Nano Lett.*, 2015, **15**, 7616–7620.
- R. Zhang, X. Wang, S. Yu, T. Wen, X. Zhu, F. Yang, X. Sun and W. Hu, *Adv. Mater.*, 2017, **29**, 1605502.
- M. A. R. Anjum and J. S. Lee, *ACS Catal.*, 2017, **7**, 3030–3038.
- P. Xiao, W. Chen and X. Wang, *Adv. Energy Mater.*, 2015, **5**, 1500985.
- D. Li, H. Baydoun, C. N. Verani and S. L. Brock, *J. Am. Chem. Soc.*, 2016, **138**, 4006–4009.
- P. He, X. Y. Yu and X. W. Lou, *Angew. Chem., Int. Ed.*, 2017, **56**, 3897–3900.
- G. Li, X. Wang, M. H. Seo, S. Hemmati, A. Yu and Z. Chen, *J. Mater. Chem. A*, 2017, **5**, 10895–10901.
- W. Gu, L. Gan, X. Zhang, E. Wang and J. Wang, *Nano Energy*, 2017, **34**, 421–427.
- B. Slijukic, D. M. Santos, M. Vujkovic, L. Amaral, R. P. Rocha, C. A. Sequeira and J. L. Figueiredo, *ChemSusChem*, 2016, **9**, 1200–1208.
- L. Han, M. Xu, Y. Han, Y. Yu and S. Dong, *ChemSusChem*, 2016, **9**, 2784–2787.
- W. Hong, J. Wang and E. Wang, *Small*, 2014, **10**, 3262–3265.
- W. Hong, C. Shang, J. Wang and E. Wang, *Energy Environ. Sci.*, 2015, **8**, 2910–2915.
- W. Hong, J. Wang and E. Wang, *ACS Appl. Mater. Interfaces*, 2014, **6**, 9481–9487.
- C. G. Morales-Guio and X. Hu, *Acc. Chem. Res.*, 2014, **47**, 2671–2681.
- L. Lin, N. Miao, Y. Wen, S. Zhang, P. Ghosez, Z. Sun and D. A. Allwood, *ACS Nano*, 2016, **10**, 8929–8937.
- L. Han, K. Feng and Z. Chen, *Energy Technol.*, 2017, DOI: 10.1002/ente.201700108.
- X. Zhang, Y. Han, L. Huang and S. Dong, *ChemSusChem*, 2016, **9**, 3049–3053.
- J. Song, C. Zhu, B. Z. Xu, S. Fu, M. H. Engelhard, R. Ye, D. Du, S. P. Beckman and Y. Lin, *Adv. Energy Mater.*, 2017, **7**, 1601555.
- M. Xu, L. Han, Y. Han, Y. Yu, J. Zhai and S. Dong, *J. Mater. Chem. A*, 2015, **3**, 21471–21477.
- Y. Li, J. Liu, C. Chen, X. Zhang and J. Chen, *ACS Appl. Mater. Interfaces*, 2017, **9**, 5982–5991.
- L. Han, S. Dong and E. Wang, *Adv. Mater.*, 2016, **28**, 9266–9291.
- T. Wu, M. Pi, D. Zhang and S. Chen, *J. Power Sources*, 2016, **328**, 551–557.
- Z. Jin, P. Li, X. Huang, G. Zeng, Y. Jin, B. Zheng and D. Xiao, *J. Mater. Chem. A*, 2014, **2**, 18593–18599.
- C. Deng, F. Ding, X. Li, Y. Guo, W. Ni, H. Yan, K. Sun and Y.-M. Yan, *J. Mater. Chem. A*, 2016, **4**, 59–66.
- H. Du, Q. Liu, N. Cheng, A. M. Asiri, X. Sun and C. M. Li, *J. Mater. Chem. A*, 2014, **2**, 14812.
- X. Wang, W. Yuan, Y. Yu and C. M. Li, *ChemSusChem*, 2017, **10**, 1014–1021.
- Y. Bai, L. Fang, H. Xu, X. Gu, H. Zhang and Y. Wang, *Small*, 2017, **13**, 1603718.

- 28 L. Han, X. Y. Yu and X. W. Lou, *Adv. Mater.*, 2016, **28**, 4601–4605.
- 29 Y. Feng, X. Y. Yu and U. Paik, *Chem. Commun.*, 2016, **52**, 1633–1636.
- 30 Y. Bai, H. Zhang, L. Liu, H. Xu and Y. Wang, *Chem.–Eur. J.*, 2016, **22**, 1021–1029.
- 31 P. Jiang, Q. Liu, C. Ge, W. Cui, Z. Pu, A. M. Asiri and X. Sun, *J. Mater. Chem. A*, 2014, **2**, 14634.
- 32 M. Liu and J. Li, *ACS Appl. Mater. Interfaces*, 2016, **8**, 2158–2165.
- 33 X. Xu, Z. Zhang and X. Wang, *Adv. Mater.*, 2015, **27**, 5365–5371.
- 34 M. Hu, S. Furukawa, R. Ohtani, H. Sukegawa, Y. Nemoto, J. Reboul, S. Kitagawa and Y. Yamauchi, *Angew. Chem., Int. Ed.*, 2012, **51**, 984–988.
- 35 M. Hu, N. L. Torad and Y. Yamauchi, *Eur. J. Inorg. Chem.*, 2012, **2012**, 4795–4799.
- 36 X. Y. Yu, L. Yu, H. B. Wu and X. W. Lou, *Angew. Chem., Int. Ed.*, 2015, **54**, 5331–5335.
- 37 J. Hao, W. Yang, Z. Zhang and J. Tang, *Nanoscale*, 2015, **7**, 11055–11062.
- 38 Z. Pu, X. Ya, I. S. Amiin, Z. Tu, X. Liu, W. Li and S. Mu, *J. Mater. Chem. A*, 2016, **4**, 15327–15332.
- 39 Y. P. Zhu, X. Xu, H. Su, Y. P. Liu, T. Chen and Z. Y. Yuan, *ACS Appl. Mater. Interfaces*, 2015, **7**, 28369–28376.
- 40 R. Jia, J. Chen, J. Zhao, J. Zheng, C. Song, L. Li and Z. Zhu, *J. Mater. Chem.*, 2010, **20**, 10829.
- 41 L. Yan, P. Dai, Y. Wang, X. Gu, L. Li, L. Cao and X. Zhao, *ACS Appl. Mater. Interfaces*, 2017, **9**, 11642–11650.